Interplay between spin-orbit couplings and residual interatomic interactions in the modulational instability of two-component Bose-Einstein condensates

Conrad Bertrand Tabi [1,*], Etienne Wamba [2,3,†], Emmanual Nare,[1,‡] and Timoléon Crépin Kofané[1,4,5,§]

[1]*Department of Physics and Astronomy, Botswana International University of Science and Technology,*
Private Mail Bag 16, Palapye, Botswana
[2]*Faculty of Engineering and Technology, University of Buea, P.O. Box 63, Buea, Cameroon*
[3]*STIAS, Wallenberg Research Centre, Stellenbosch University, Stellenbosch 7600, South Africa*
[4]*Laboratory of Mechanics, Department of Physics, Faculty of Science, University of Yaoundé I, P.O. Box 812, Yaoundé, Cameroon*
[5]*Centre d'Excellence Africain en Technologies de l'Information et de la Communication, University of Yaoundé I, Yaoundé, Cameroon*

The nonlinear dynamics induced by the modulation instability (MI) of a binary mixture in an atomic Bose-Einstein condensate (BEC) is investigated theoretically under the joint effects of higher-order residual nonlinearities and helicoidal spin-orbit (SO) coupling in a regime of unbalanced chemical potential. The analysis relies on a system of modified coupled Gross-Pitaevskii equations on which the linear stability analysis of plane-wave solutions is performed, from which an expression of the MI gain is obtained. A parametric analysis of regions of instability is carried out, where effects originating from the higher-order interactions and the helicoidal spin-orbit coupling are confronted under different combinations of the signs of the intra- and intercomponent interaction strengths. Direct numerical calculations on the generic model support our analytical predictions and show that the higher-order interspecies interaction and the SO coupling can balance each other suitably for stability to take place. Mainly, it is found that the residual nonlinearity preserves and reinforces the stability of miscible pairs of condensates with SO coupling. Additionally, when a miscible binary mixture of condensates with SO coupling is modulationally unstable, the presence of residual nonlinearity may help soften such instability. Our results finally suggest that MI-induced formation of stable solitons in mixtures of BECs with two-body attraction may be preserved by the residual nonlinearity even though the latter enhances the instability.

I. INTRODUCTION

The experimental realization of atomic gas Bose-Einstein condensates (BECs) has provided new opportunities for the study of quantum phenomena on a mesoscopic scale. Quantitative measurements of collective excitations [1–6], sound propagation [7], and interactions between distinct condensates [8,9] have been made. It is now well accepted that, for sufficiently low temperatures, the nonlinear properties of atomic matter waves are well described by the time-dependent Gross-Pitaevskii (GP) nonlinear equation, which takes trapping potentials, spatial distributions of macroscopic wave functions for the mean-field condensates, and interatomic interactions into account [10,11]. In addition, the GP equation includes a two-body nonlinear term through a contact interaction that is parametrized by the *s*-wave scattering length, which determines the nonlinearity strength in the mean-field description of the condensate and can be manipulated by the magnetically [12], optically [13], or confinement-induced [14] Feshbach resonance.

In this respect, several remarkable results on nonlinear excitations have been reported theoretically as well as experimentally. They include the four-wave mixing in BECs [15], vortices [16–18]; dark solitons in BECs [19,20]; bright solitons [21]; multisoliton complexes [22]; compactons [23]; nonlinear periodic waves [24]; gray solitons [25]; gap matter solitons [26]; Faraday waves [27]; Bloch oscillations of BECs; Landau-Zener tunneling [28], superfluid to Mott insulator phase transition [29]; compression of a condensate [30]; temporal [31], spatial [32,33], and spatiotemporal chaos [34,35], the process of BEC collapse [36]; and open BECs [37,38].

Modulational instability (MI), in which small perturbations to a carrier wave, reinforced by nonlinearity, experience rapid growth [39], is an indispensable mechanism for understanding pattern formation in a uniform medium. The MI in two-component BECs was first discussed by Goldstein and Meystre [40]. Following these studies, the MI in two-component BEC systems has been studied extensively [41–43]. Indeed, MI-induced regular density modulations, formed throughout the BEC, lead to the emergence of a large number of beating dark-dark solitons [44], static dark-dark solitons [45], and dark-bright solitons [46].

Recently, the further development of trapping techniques has allowed the creation of multicomponent condensates, which are formed by trapping different atomic species or the same atoms with different hyperfine spin states [8,47].

*tabic@biust.ac.bw
†ettienne.wamba@ubuea.cm
‡emmanuel.nare@studentmail.biust.ac.bw
§tckofane@yahoo.com

In multicomponent systems, additional types of interactions, such as interspecies interactions, can occur between different components of the condensates leading to new features not observable in a single condensate. Among these features, we have complex phase diagrams [48–51], metastable states [52], vortex transfer dynamics [16,50], and symmetry-breaking instabilities [53,54]. In addition, the interaction between half-quantum vortices [55], reconnection of $\frac{1}{3}$ vortices [56], the dynamics of spin-vortex dipoles [57], and the collision of skyrmions, scattering dynamics of skyrmions, and generation of multiple skyrmions [58] have been predicted. The collision of half-quantum vortices in a spin-1 BEC was also observed [59,60]. Countersuperflow instability has been studied theoretically [46,61], as well as experimentally [62] in mixed BECs of cold atoms by accelerating the two components in opposite directions, utilizing the Zeeman shift under a magnetic-field gradient.

Spin-orbit (SO)-coupled BECs have been studied extensively in different contexts, including phase separation, stripe phases [63], spotlighting the phase transition [64], and vortices with or without rotations [65,66]. In addition, the MI in two-component BECs with SO coupling in one [67–69] and two dimensions [70] was recently explored. Indeed, the effects of the MI on the ferromagnetic ground state of the trapped spinor BEC modeled by three coupled field equations have been studied analytically and demonstrated numerically [71]. The spontaneous multidomain formation induced by the dynamical instability in a spin-1 condensate with ferromagnetic interactions has been investigated through extensive numerical simulations [72]. A complete understanding of domain formation in a spin-1 atomic condensate has been provided [73]. It has been observed that the MI phenomenon can lead the sound waves propagating in continuous-wave solutions of repulsive spinor BECs to the exponential growth of noise and that this can eventually destroy the initial underlying continuous wave and create a spin texture [74]. Conditions of MI in one-dimensional (1D) effective one-component quantum droplets and Bose-Bose mixtures, coupled through SO and Rabi couplings, have been established [75].

The objective of the present work is to study the mechanism of MI of the two-component helicoidal SO-coupled BECs equally distributed between the two pseudospin states, in a steady-state propagation regime, taking into account the residual nonlinearity describing the shape-dependent confinement correction of the two-body collision potential. It has been shown that higher-order interactions induced by shape-dependent confinement can either suppress or enhance the MI, which is interesting for control of one-component BEC instabilities [76]. In the two-component BECs, the space-time evolution of the density shows that the residual nonlinearity may play an important role in producing the MI conditions in miscible condensates and altering the MI conditions in immiscible condensates at appropriate physical settings [77].

The rest of the paper is organized as follows. In Sec. II we formulate the problem for two-component BECs using a system of 1D coupled GP equations that account for the helicoidal SO-coupling with residual nonlinearity. In Sec. III we undertake the linear stability of plane-wave solutions of the proposed model equations. The instability zones, as well as the analytical expressions of the gain of MI, are obtained. In Sec. IV the results of linear stability analysis are validated by the direct numerical simulations of the governing equation using the split-step Fourier transform method. The emergence of matter waves in binary BECs is comprehensively discussed. The joint effect of helicoidal SO coupling and higher-order residual interaction strengths, under different combinations of intra- and intercomponents of interaction strengths, is also regarded. Section V summarizes the paper and gives possible future directions.

II. THEORETICAL MODEL AND LINEAR STABILITY ANALYSIS

A. Theoretical model

In the present paper, interested in the interplay between shape-dependent confinement and spin-orbit coupling in the generation of nonlinear excitations, we adopt as a governing model a vector Gross-Pitaevskii equation with residual nonlinearities and spin-momentum coupling terms. In such a context of mean-field approximation, with macroscopic wave functions of macroscopic quantum states of the two-component condensate with spin-up and spin-down internal states and with helicoidal SO coupling, the vector Gross-Pitaevskii equation with spin-orbit coupling reads [78]

$$i\frac{\partial \Psi}{\partial t} = -\frac{1}{2}\Psi_{xx} + i(\beta\sigma_z - \alpha\sigma_x)\Psi_x + \frac{\Delta}{2}\sigma_z\Psi$$
$$+ \begin{pmatrix} \Psi^\dagger G_1 \Psi & 0 \\ 0 & \Psi^\dagger G_2 \Psi \end{pmatrix}\Psi$$
$$+ \begin{pmatrix} (\Psi^\dagger P_1 \Psi)_{xx} & 0 \\ 0 & (\Psi^\dagger P_2 \Psi)_{xx} \end{pmatrix}\Psi, \tag{1}$$

where $\Psi = (\psi_1, \psi_2)^T$, $G_i = \begin{pmatrix} g_i & 0 \\ 0 & g_{i,3-i} \end{pmatrix}$, and $P_i = \begin{pmatrix} p_i & 0 \\ 0 & p_{i,3-i} \end{pmatrix}$, with $i = 1, 2$. The $\sigma_{x,z}$ are Pauli matrices. This model originates from a modified GP equation that contains higher-order (HO) terms and a multichannel model of Feshbach resonances [79]. Based on that modified GP equation, a set of coupled GP equations was derived to describe a binary mixture of 1D BEC condensates in the presence of HO residual nonlinearities [77]. Recently, in the context of MI, it was shown that matter waves arise even in the miscible binary BECs due to the helicoidal SO interaction [68,69]. In a situation where the scattering dynamics is involved, the HO correction should be considered. Such terms in the GP equation account for Rydberg molecules embedded in the condensate [80] and for narrow Feshbach resonances and tighter traps [79], known to enhance the condensate stability [79]. In a more explicit form, the ruling equations for the dynamics of macroscopic wave functions of the two-component condensate are the coupled 1D cubic GP equations

$$i\frac{\partial \psi_1}{\partial t} = -\frac{1}{2}\frac{\partial^2 \psi_1}{\partial x^2} + i\beta\frac{\partial \psi_1}{\partial x} - i\alpha\frac{\partial \psi_2}{\partial x} + \frac{\Delta}{2}\psi_1$$
$$+ (g_1|\psi_1|^2 + g_{12}|\psi_2|^2)\psi_1$$
$$+ \left(p_1\frac{\partial^2|\psi_1|^2}{\partial x^2} + p_{12}\frac{\partial^2|\psi_2|^2}{\partial x^2}\right)\psi_1, \tag{2}$$

$$i\frac{\partial \psi_2}{\partial t} = -\frac{1}{2}\frac{\partial^2 \psi_2}{\partial x^2} - i\beta\frac{\partial \psi_2}{\partial x} - i\alpha\frac{\partial \psi_1}{\partial x} - \frac{\Delta}{2}\psi_2$$
$$+ (g_2|\psi_2|^2 + g_{21}|\psi_1|^2)\psi_2$$
$$+ \left(p_2\frac{\partial^2|\psi_2|^2}{\partial x^2} + p_{21}\frac{\partial^2|\psi_1|^2}{\partial x^2}\right)\psi_2, \qquad (3)$$

where ψ_1 and ψ_2 are the two-component BECs pseudospin states, β is the helicoidal gauge potential, α represents the SO coupling, and Δ is the strength of the Zeeman splitting. Next, $g_1 = 2a_{11}/a_\perp$ and $g_2 = 2a_{22}/a_\perp$ are the strengths of the two-body intraspecies interactions, while $g_{12} = 2a_{12}/a_\perp$ and $g_{21} = 2a_{21}/a_\perp$ denote the strengths of the two-body interactions. The p_1 and p_2 are the intraspecies and p_{12} and p_{21} the interspecies higher-order interaction strengths, respectively. In the present work we assume that the interspecies interaction parameters are the same $g_{12} = g_{21}$. Here $a_\perp = \sqrt{\hbar/mw_\perp}$ is the transverse characteristic length, $w_\perp$ is the transverse trap frequency, m is the atomic mass, and $\hbar$ is the Planck constant. The a_{11}, a_{22}, and a_{12} are three s-wave scattering lengths, which in principle can be independently adjusted in experiments using optical and magnetic Feshbach resonance techniques [12,81,82]. In practice, however, one scattering length is generally fixed while the two others are tuned simultaneously [83,84]. Finally, the spatial variable x, time t, density $|\psi_1|^2 + |\psi_2|^2$, and energy are expressed in normalized units $a_\perp$, $\omega_\perp^{-1}$, $a_\perp^{-1}$, and $\hbar\omega_\perp$, respectively. The wave functions are normalized by the respective atom numbers $N_j = \int(|\psi_j|^2 dx)$ with $j = 1, 2$.

B. Linear stability analysis and eigenfrequencies of unstable modes

In order to study the MI of Eqs. (2) and (3), we use the standard linear stability analysis. For this, we consider the propagation of the cw or quasi-cw state in the form of miscible binary condensate with uniform densities n_{10} and n_{20} and the common chemical potential μ of both components. The steady-state solutions of a system of two coupled 1D cubic GP equations with helicoidal coupling and higher-order residual nonlinearity, corresponding to the cw state, can be written as

$$\psi_j = e^{-i\mu_j t}\sqrt{n_{j0}}, \quad j = 1, 2. \qquad (4)$$

The densities, Zeeman splitting, SO coupling, higher-order residual nonlinearity, intraspecies and interspecies interactions, and chemical potential are determined by algebraic equations

$$\mu_j = \frac{(-1)^{j-1}\Delta}{2} + g_j n_{j0} + g_{12}n_{3-j,0}. \qquad (5)$$

In order to investigate the MI of BECs with helicoidal SO coupling and higher-order residual nonlinearity, we introduce the perturbed field of the form

$$\psi_j = e^{-i\mu_j t}(\sqrt{n_{j0}} + \delta\psi_j), \quad j = 1, 2, \qquad (6)$$

where the complex fields $\delta\psi_j \equiv \delta\psi_j(x, t)$ represent small perturbations such that $|\delta\psi_j| \ll \sqrt{n_{j0}}$. Substituting Eq. (6) into

(2) and (3) and linearizing around the unperturbed solutions leads to the equations for the perturbed fields

$$i\frac{\partial}{\partial t}(\delta\psi_1) = -\frac{1}{2}\frac{\partial^2}{\partial x^2}(\delta\psi_1) + i\beta\frac{\partial}{\partial x}(\delta\psi_1) - i\tilde{\alpha}\frac{\partial}{\partial x}(\delta\psi_2)$$
$$+ n_{10}\left(g_1 + p_1\frac{\partial^2}{\partial x^2}\right)(\delta\psi_1^* + \delta\psi_1)$$
$$+ \sqrt{n_{10}n_{20}}\left(g_{12} + p_{12}\frac{\partial^2}{\partial x^2}\right)(\delta\psi_2^* + \delta\psi_2), \quad (7)$$

$$i\frac{\partial}{\partial t}(\delta\psi_2) = -\frac{1}{2}\frac{\partial^2}{\partial x^2}(\delta\psi_2) - i\beta\frac{\partial}{\partial x}(\delta\psi_2) - i\tilde{\alpha}^*\frac{\partial}{\partial x}(\delta\psi_1)$$
$$+ n_{20}\left(g_2 + p_2\frac{\partial^2}{\partial x^2}\right)(\delta\psi_2^* + \delta\psi_2)$$
$$+ \sqrt{n_{20}n_{10}}\left(g_{12} + p_{12}\frac{\partial^2}{\partial x^2}\right)(\delta\psi_1^* + \delta\psi_1), \quad (8)$$

where $\delta\psi_j^*$ are the complex conjugates of the perturbed fields $\delta\psi_j$ and $\tilde{\alpha} \equiv \tilde{\alpha}(t) = \alpha e^{i\kappa t}$. The frequency term is given by

$$\kappa = \mu_1 - \mu_2 = n_{10}(g_1 - g_{12}) - n_{20}(g_2 - g_{12}) + \Delta \qquad (9)$$

and then represents an imbalance between the chemical potentials of the two condensates. Now we assume the following ansatz for the perturbed fields:

$$\delta\psi_j = \zeta_j \cos\left(kx - \int_0^t \Omega(s)ds\right)$$
$$+ i\eta_j \sin\left(kx - \int_0^t \Omega(s)ds\right). \qquad (10)$$

Here k is a real wave number, Ω is a complex eigenfrequency, and ζ_j and η_j are amplitudes. A set of linearly coupled equations for perturbation amplitudes ζ_j and η_j are derived by substituting Eq. (10) in Eqs. (7) and (8),

$$\mathbf{M} \times (\zeta_1, \zeta_2, \eta_1, \eta_2)^T = 0, \qquad (11)$$

where $\mathbf{M}$ is a 4×4 matrix. There exists a nontrivial solution under the condition that $\det(\mathbf{M}) = 0$ and in such a case we can obtain the dispersion relation of the system for Ω. The matrix $\mathbf{M}$ is expressed as

$$\mathbf{M} = \begin{pmatrix} \Omega + \omega_{11} & \omega_{12} & \omega_{13} & \omega_{14} \\ \omega_{21} & \Omega + \omega_{22} & \omega_{23} & \omega_{24} \\ \omega_{31} & \omega_{32} & \Omega - \omega_{33} & \omega_{34} \\ \omega_{41} & \omega_{42} & \omega_{43} & \Omega - \omega_{44} \end{pmatrix}, \quad (12)$$

with the entries given by

$$\omega_{11} = \omega_{22} = \omega_{33} = \omega_{44} = \beta k,$$
$$\omega_{12} = -\frac{k^2}{2}, \quad \omega_{13} = -\tilde{\alpha}k, \quad \omega_{14} = 0,$$
$$\omega_{21} = -2n_{10}(g_1 - k^2 p_1) - \frac{k^2}{2},$$
$$\omega_{23} = 2\sqrt{n_{10}n_{20}}(k^2 p_{12} - g_{12}),$$
$$\omega_{24} = \omega_{31} = \omega_{13}, \quad \omega_{32} = 0,$$
$$\omega_{34} = \omega_{12}, \quad \omega_{41} = 2\sqrt{n_{10}n_{20}}(k^2 p_{21} - g_{21}),$$
$$\omega_{42} = \omega_{13}, \quad \omega_{43} = -2n_{20}(g_2 - k^2 p_2) - \frac{k^2}{2}. \qquad (13)$$

From the structure of the matrix, it is natural to set $\gamma_j = g_j - p_j k^2$ ($j = 1, 2$) and $\gamma_{12} = g_{12} - p_{12} k^2$ as the effective strengths of intra- and intercomponent two-body interactions, respectively. A nontrivial solution of a system of four equations requires that $\det(\mathbf{M}) = 0$. After some straightforward calculations, we obtain the nonlinear dispersion relation

$$\Omega^4 + C_2\,\Omega^2 + C_1\,\Omega + C_0 = 0, \tag{14}$$

where the coefficients C_n ($n = 0, 1, 2$) are given by

$$C_2 = -k^2\left(2(\alpha^2 + \beta^2) + \gamma_2 n_{20} + \gamma_1 n_{10} + \frac{k^2}{2}\right),$$

$$C_1 = -2k^3[\beta(\gamma_2 n_{20} - \gamma_1 n_{10}) + 2\tilde{\alpha}_r\sqrt{\gamma_{12}\gamma_{21}n_{10}n_{20}}],$$

$$C_0 = \frac{k^4}{16}\{[k^2 - 4(\alpha^2 + \beta^2 - \gamma_1 n_{10})]$$
$$\times [k^2 - 4(\alpha^2 + \beta^2 - \gamma_2 n_{20})] - 16\gamma_{12}\gamma_{21}n_{10}n_{20}\}, \tag{15}$$

with $\tilde{\alpha}_r \equiv \alpha\cos(\kappa t)$. Then the corresponding SO coupling coefficient turns out to be varying periodically in time. The four solutions obtained from Eq. (14) are

$$\Omega_{1,2} = -\Omega_0 \pm \frac{1}{2}\sqrt{-2(C_2 + 2\Omega_0^2) + \frac{C_0}{\Omega_0}},$$

$$\Omega_{3,4} = \Omega_0 \pm \frac{1}{2}\sqrt{-2(C_2 + 2\Omega_0^2) - \frac{C_0}{\Omega_0}}, \tag{16}$$

where $\Omega_0 = \frac{1}{2}\sqrt{\Lambda - \frac{2}{3}C_2}$, with $\Lambda = \frac{1}{3}(\Lambda_0 + \frac{\Delta_1}{\Lambda_0})$ and $\Lambda_0 = (\frac{\Delta_2 + \sqrt{\Delta_2^2 - 4\Delta_1^3}}{2})^{1/3}$ for $\Delta_1 = C_2^2 + 12C_0$ and $\Delta_2 = 2C_2^3 + 27C_1^2 - 72C_2C_0$. These time-dependent frequencies are very important in analyzing the MI onset because they provide the instability criteria of the system. In problems with time-dependent Hamiltonians, quasienergies may become time dependent, especially in unstable regimes. Such time-dependent quasienergies can be measured accurately in atoms using transient absorption spectroscopy, as it has been demonstrated recently [85].

C. Eigenfrequencies of unstable modes in the limit of large chemical potential imbalance

In the preceding section the system of equations (7) and (8) actually represents a Floquet problem, which has the form

$$i\frac{\partial\delta\psi}{\partial t} = H(t)\delta\psi, \tag{17}$$

where $\delta\psi = (\delta\psi_1, \delta\psi_2)^T$ and

$$H = -\frac{1}{2}\frac{\partial^2}{\partial x^2} + i(\beta\sigma_z - \alpha\sigma)\frac{\partial}{\partial x} + \left(\mathbf{g} + \mathbf{q}\frac{\partial^2}{\partial x^2}\right)\mathbf{c}. \tag{18}$$

In this equation the linear operator $\mathbf{c}$ is defined such that $\mathbf{c}[\delta\psi] = \delta\psi + \delta\psi^*$. We have $\sigma \equiv \sigma(t) = \sigma_x\cos(\kappa t) - \sigma_y\sin(\kappa t)$ and the matrices

$$\mathbf{g} = \begin{pmatrix} n_{10}g_1 & \sqrt{n_{10}n_{20}}g_{12} \\ \sqrt{n_{10}n_{20}}g_{12} & n_{20}g_2 \end{pmatrix},$$

$$\mathbf{q} = \begin{pmatrix} n_{10}p_1 & \sqrt{n_{10}n_{20}}p_{12} \\ \sqrt{n_{10}n_{20}}p_{12} & n_{20}p_2 \end{pmatrix}. \tag{19}$$

The coefficients σ_x, σ_y, and σ_z are Pauli matrices. Since $H(t)$ is a time-dependent function such that $H(t + T) = H(t)$, with period $T = 2\pi/\kappa$, the energy of the system is no longer conserved and thus becomes undefined. It is replaced by a quasienergy which is unique up to multiples of $\hbar\kappa$, where κ plays the role of the driving frequency. In the limit of large driving frequencies, quasienergies are obtained through the averaged energy in Floquet states. The useful analytical tool for deriving the Floquet Hamiltonian is the Magnus expansion, which in this case of periodically driven systems is referred to as the Magnus-Floquet expansion [86,87]. In general, this expansion is used for finding the Floquet Hamiltonian when there is a time-varying external potential in the usual physical space (see, for instance, Refs. [88–92]). In our setting (7) and (8), however, the periodic driving happens to apply to a momentum term, yielding a kinematic momentum, which makes it very hard to treat in position space, and switching to the rotating frame [78] or using more sophisticated gauge transformations may not solve the problem. In order to circumvent that difficulty, it is appropriate to solve the system in momentum space. Taking the Fourier transform of Eq. (17) over the spatial domain x, we get

$$i\frac{\partial\widehat{\delta\psi}}{\partial t} = \mathcal{H}(t)\widehat{\delta\psi}, \tag{20}$$

where $\widehat{\delta\psi} \equiv \widehat{\delta\psi}(k, t) = (\delta\hat{\psi}_1, \delta\hat{\psi}_2)^T$ is the Fourier transform of the perturbation $\delta\psi(x, t)$ over the spatial domain x, and denoting the spatial frequency as k, we get

$$\mathcal{H}(t) = \frac{1}{2}k^2 - [\beta\sigma_z - \alpha\sigma(t)]k + (\mathbf{g} - \mathbf{q}k^2)\mathbf{c}.$$

The dynamics induced by the varying Hamiltonian part in the system can be given, to the first order, by the leading contribution to the Floquet-Magnus expansion. It is ruled by the unitary transformation [87]

$$U = \exp\left(-i\frac{\alpha k}{\kappa}[\sigma_x\sin(\kappa t) + \sigma_y\cos(\kappa t) - \sigma_y]\right).$$

The operator U can help us understand the effect of periodic drives on dynamical instabilities. The transformed Hamiltonian, given by $\tilde{\mathcal{H}} = U^\dagger[\mathcal{H}(t) - i\frac{\partial}{\partial t}]U$, is found to be

$$\tilde{\mathcal{H}} = \frac{k^2}{2} - \frac{\beta(\zeta_1\,\sigma_y k^2 - \zeta_2\,\sigma_x k^2 + \sigma_z k)}{1 + \frac{16\alpha^2 k^2}{\kappa^2}\sin^2(\kappa t/2)} + (\mathbf{g} - \mathbf{q}\,k^2)\mathbf{c}, \tag{21}$$

where $\zeta_1(t) = 2\frac{\alpha}{\kappa}\sin(\kappa t)$ and $\zeta_2(t) = 2\frac{\alpha}{\kappa}[\cos(\kappa t) - 1]$. Therefore, the effective Hamiltonian, obtained by averaging $\tilde{\mathcal{H}}$ over a period, reads

$$\tilde{\mathcal{H}}_{\text{eff}} = \frac{k^2}{2} + v_1\sigma_x - v_2\sigma_z + (\mathbf{g} - \mathbf{q}\,k^2)\mathbf{c}, \tag{22}$$

where $v_1 = \frac{\kappa\beta[1-\sqrt{1+(\frac{4\alpha}{\kappa})^2 k^2}]}{4\alpha\sqrt{1+(\frac{4\alpha}{\kappa})^2 k^2}}$ and $v_2 = \frac{\beta k}{\sqrt{1+(\frac{4\alpha}{\kappa})^2 k^2}}$. In the limit when $\alpha/\kappa \to 0$, we get $v_1 \to 0$ and $v_2 \to \beta k$. Let us decompose the perturbation $\delta\psi$ into real and imaginary parts, i.e., $\delta\psi = \varphi_r + i\varphi_i$. Then if we set $\widehat{\delta\psi} = \hat{\varphi}_r + i\hat{\varphi}_i$, with $\hat{\varphi}_r = (\hat{\varphi}_{1r}, \hat{\varphi}_{2r})^T$ and $\hat{\varphi}_i = (\hat{\varphi}_{1i}, \hat{\varphi}_{2i})^T$, the dynamics of the system in the large imbalance limit is well described by the effective Schrödinger equation $i\partial_t\widehat{\delta\psi} = \tilde{\mathcal{H}}_{\text{eff}}\widehat{\delta\psi}$ or equivalently by a

matrix equation of the form

$$\frac{\partial \hat{\varphi}}{\partial t} = \mathcal{M}\hat{\varphi}, \qquad (23)$$

where the vector $\hat{\varphi} = (\hat{\varphi}_{1r}, \hat{\varphi}_{1i}, \hat{\varphi}_{2r}, \hat{\varphi}_{2i})^T$ and the matrix $\mathcal{M}$ reads

$$\mathcal{M} = \begin{pmatrix} 0 & \frac{1}{2}k^2 - v_2 & 0 & v_1 \\ v_2 + \omega_{21} & 0 & -v_1 + \omega_{23} & 0 \\ 0 & v_1 & 0 & \frac{1}{2}k^2 + v_2 \\ -v_1 + \omega_{41} & 0 & -v_2 + \omega_{43} & 0 \end{pmatrix}. \qquad (24)$$

The parameters ω_{ij} are the same as in the preceding section. The four eigenvalues of the matrix $\mathcal{M}$ are given by

$$\lambda_{\pm}^2 = \tfrac{1}{2}(C \pm \sqrt{C^2 - 4D}), \qquad (25)$$

where the coefficients are given by $C = \frac{1}{2}(\omega_{43} + \omega_{21})k^2 + v_2(\omega_{43} - \omega_{21}) - 2(v_1^2 + v_2^2 - v_1\omega_{23})$ and $D = (v_1^2 + v_2^2 - \frac{1}{4}k^4)[(v_1 - \omega_{23})^2 + v_2^2 - v_2(\omega_{43} - \omega_{21}) - \omega_{43}\omega_{21}]$.

III. ANALYSIS OF THE INSTABILITY ONSET: INSTABILITY GAINS AND DOMAINS

From the above perturbation frequencies, we can get considerable insight into the dynamical behavior of the system, notably the stable and unstable domains as well as the corresponding instability gains.

A. Instability growth rate

The set of solutions (16) implies that Ω may be positive, negative, or even complex, depending on the system parameters. However, real, negative, or positive, values of Ω predict the stability of the cw. General complex solutions of Eq. (14) are such that $\Omega = \Omega_r + i\Omega_i$ so that $\exp(-i \int \Omega \, dt) = \exp(-i \int \Omega_r dt) \exp(\int \Omega_i dt)$. This means that the occurrence of instability fully depends on the imaginary part of the perturbation frequency.

In the particular case when the two BEC components have a common chemical potential, the parameters Δ, n_{0j}, g_j, and g_{12} satisfy the relation

$$\Delta - [n_{20}(g_2 - g_{12}) - n_{10}(g_1 - g_{12})] = 0, \qquad (26)$$

and we obviously have $\kappa = 0$, because $\mu_1 = \mu_2$. Then $\tilde{\alpha}^* = \tilde{\alpha} = \alpha$ and Ω is time independent. For two BEC components with equal densities $n_{01} = n_{02} = n_0$, for instance, the above condition merely reduces to taking $\Delta = n_0(g_2 - g_1)/2$. In such a case, necessary information about the instability of the system can be extracted through the maximum MI growth rate given by

$$\xi(\Omega) = [|\text{Im}(\Omega)|]_{\text{max}}, \qquad (27)$$

where the maximum is obviously taken over all perturbation frequencies Ω_j ($j = 1, \ldots, 4$). In practice, however, it is not obvious how to fulfill the condition (26) exactly because of inevitable errors and deviations.

In the general case where the physical system's parameters Δ, n_{0j}, g_j, and g_{12} are chosen freely, it is completely unrealistic to neglect the imbalance κ between the components of

the binary mixture. To better quantify the MI growth rate, we introduce the so-called integrated gain defined as a functional of the time-dependent perturbation frequency Ω and given by

$$G[\Omega] = [|\text{Im}(\omega)|]_{\text{max}}, \qquad (28)$$

where the complex frequency

$$\omega(\tau) = \frac{1}{\tau} \int_0^{\tau} \Omega(t)dt. \qquad (29)$$

The bound $\tau \in \,]0, t_{\text{max}}]$ is any realistic timescale over which MI is expected to develop in the system, with t_{max} the run time of the experiment. In the case when the chemical potential imbalance $\kappa = 0$ or in the limit $\tau \to 0$, we readily get the standard case $G = \xi \equiv [|\text{Im}(\Omega)|]_{\text{max}}$. There is a possibility for the integrated gain (28) to be directly measured in any cold-atom experiment (see Ref. [93]). The process would be the following. Let the BEC evolve in an external potential (magnetic trap and optical lattice) for a variable time $t \geqslant t_0$. Then switch off the potential, let the free BEC expand, and image the atomic cloud to get the number of atoms $N(t)$. When the physical system has no time-dependent parameter, the result $\ln[N(t)/N(t_0)]$ can be linearly fitted to γt, which means we have purely exponential growth. Then the growth rate is simply extracted as the loss rate γ. When the physical system is subject to dynamical effects, like time management of parameters, we expect the result $\ln[N(t)/N(t_0)]$ to be fitted to a curve $\Gamma(t)$, where $\Gamma(t)$ is not necessarily a linear function of t. In that case the growth rate can be extracted as the time average of all loss rates measured through linear fits at different times.

In the limit of large chemical potential imbalance, the system becomes unstable when at least one of the eigenfrequencies (25) acquires a positive real part. It is therefore sufficient to have $\lambda_{\pm}^2$ positive for the condensates to undergo modulational instability. The MI gain in this case is expressed in terms of $|\text{Re}(\lambda_{\pm})|$, from which we define the total growth rate to be

$$\xi(\lambda) = [|\text{Re}(\lambda_{\pm})|]_{\text{max}}. \qquad (30)$$

Note that this growth rate is obtained from the real parts of the eigenvalues.

B. Gain profiles and instability domains

The linear stability analysis is crucial to the study of the emergence of matter waves in the sense that it gives some onset of MI. The detected regions of parameters will allow proceeding with numerical simulations with accuracy. In general, predictions of MI rely on its growth rate, which can be obtained numerically or analytically. As stated earlier, depending on the chemical potentials of the two components, when $\kappa \to 0$, the chemical imbalance is weak, i.e., $\mu_1 \approx \mu_2$. The MI growth rate can be directly plotted from the formula $G = [|\text{Im}(\Omega)|]_{\text{max}}$, obtained from Eq. (16). On the other side, for $\kappa \neq 0$, the imbalance between the chemical potentials of the two components imposes the use of the formula (30). Nevertheless, the growth rate of MI, in general, contains nonlinear and dispersive terms whose suitable balance is confronted by the effect of the helicoidal SO coupling, materialized by α and β. In the process, additional nonlinear effects are introduced
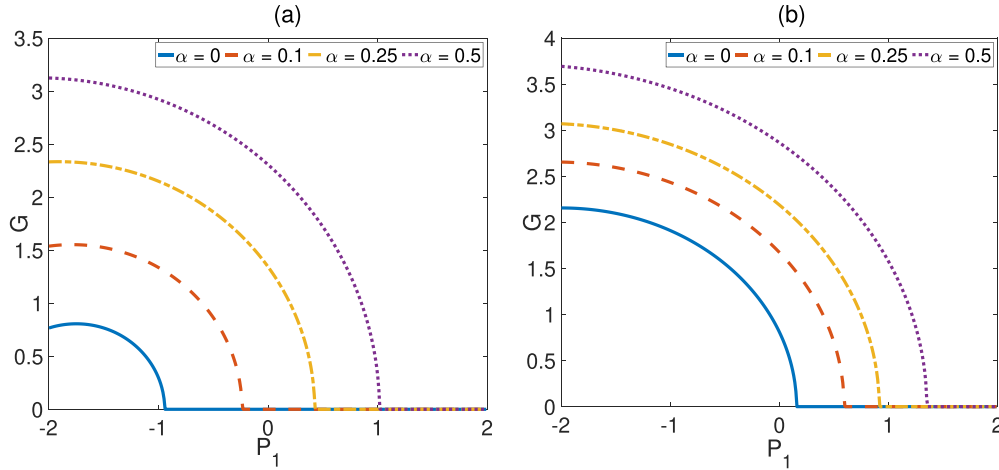
FIG. 1. Variation of the MI growth rate versus the intraspecies higher-order interaction under the effect of the helicoidal SO coupling for $g_1 = 4$, $g_2 = 1$, and $g_{12} = 0.5$: (a) the helicoidal gauge potential is switched off $\beta = 0$ and G evolves with changing α and (b) $\beta \neq 0$ ($\beta = 0.5$) and α changes the same way as in (a).

by the HO interaction terms that are different in the model studied. In the rest of this section, the growth rate spectrum is addressed separately for each of the cases.

1. Case of weak chemical potential imbalance

It is primordial to estimate values that are likely to support the emergence of nonlinear patterns in the growth rate spectrum. This is illustrated in Fig. 1, where the integrated gain of instability is plotted against the intraspecies HO interaction strength $P_1 = P_2$ in the absence [see Fig. 1(a)] and presence [see Fig. 1(b)] of the helicoidal gauge potential β. Precisely, for $P_1 = P_2 = P_{12} = P_{21} = 0$ and $\mu_1 = \mu_2$, one recovers the dispersion relation from Ref. [68], which does not include any timescale over which the MI gain is expected to develop. Additionally, if $\alpha = \beta = 0$, the commonly known case of MI is recovered. However, with $P_1 = P_2 \neq 0$, the features of Fig. 1(a) reveal the presence of MI when $\alpha = \beta = 0$, except that only negative values of P_1 contribute to the development of the instability. In the meantime, with $\alpha \neq 0$ and increasing, the instability region diffuses toward positive values of P_1, which gives more room for the HO interaction coefficients to contribute to the onset of MI and justifies the importance of the helicoidal SO coupling in the process. The same behavior of the MI gain remains ostensible even for $\beta \neq 0$ [see Fig. 1(b)]. To proceed further, we introduce $P_{ij} = g_0 g_{ij}$, where g_0 is positive for all kinds of interactions.

Recall that the main difference of the model under study is the combination of HO interatomic interactions and the helicoidal SO coupling. Note that the difference between the chemical potentials of the two species introduces a timescale for the MI gain to be computed. It is fixed, for the rest of this analysis, as $t_{max} = 5$. In Fig. 2 the stability and instability features are displayed in the (α, β) plane, where Fig. 2(a) show G for $g_1 > g_2$ and $g_{12} = 0$, with g_0 taking the values 0 [Fig. 2(a1)], 0.24 [Fig. 2(a 2)], and 0.90 [Fig. 2(a3)]. Here $g_0 = 0$ gives results from Ref. [68], which does not include the HO interactions, while $g_0 \neq 0$ implies the presence of such interactions. In general, the MI regions are of a crescent shape and symmetrical with respect to the $\alpha = 0$ axis. The

parametric expansion of the MI zone decreases with increasing g_0, i.e., the strength of the HO interatomic interactions. The same scenario is visible when $g_{12} \neq 0$ and $g_1 = g_2 = 4$, as depicted in Fig. 2(b). However, even though the point $(\alpha, \beta) = (0, 0)$ remains a stable point, the symmetry of the instability regions appears with respect to the $\beta = 0$ axis, which also means instability for both left- and right-handed SO coupling.

To further explore the contribution of the helicoidal SO coupling versus the effect of the residual nonlinearities, more results are summarized in Figs. 3 and 4, under the respective conditions $g_1 g_2 > g_{12}^2$ and $g_1 g_2 = g_{12}^2$, for different combinations of the interatomic interaction strengths. In particular, the cases $g_1 > g_2$ and $g_1 < g_2$ are compared to the features of instability due to $g_1 = g_2$. Interestingly, the instability gain highly depends on the excitation wave number whose variations induce a rich MI cascade scenario. In the first case, for example, the presence of the residual nonlinearities, with $g_0 = 0.02$, breaks the MI gain of Fig. 2(a1) into four pieces, with regions of high intensity belonging to zones where α and β are both positive [see Fig. 3(a$_1$)]. With increasing the wave number k to 3, the crescent shapes of instability appear and the four instability regions are shifted with respect to $(\alpha, \beta) = (0, 0)$ along the α axis. When $k = 5$, only two symmetrical regions of instability remain, separated by the $\alpha = 0$ axis [see Fig. 3(a$_3$)]. For $g_1 = g_2$, still under the miscibility condition, one sees two symmetrical regions of instability along the α axis, in the presence of two minor axes [see Fig. 3(b$_1$)]. Imposing $k = 3$, the two spots of high intensity are reduced [see Fig. 3(b$_2$)], a behavior that gets pronounced for $k = 5$, with a slight clockwise rotation around $(\alpha, \beta) = (0, 0)$, as shown in Fig. 3(b$_3$). For the case $g_1 < g_2$ [see Fig. 3(c)], regions of high MI gain appear where the signs of α and β are opposite, after a counterclockwise rotation compared Fig. 3(b$_1$), while regions with low intensity belong to the interval of α and β with identical signs. We should stress that this case, where $k = 1$, is the opposite of what is obtained for $g_1 > g_2$. In Fig. 3(c$_2$), where $k = 3$, the intensity of MI is amplified and keeps the same parametric distribution. In general, Fig. 3 shows that the MI gain is amplified gradually and the regions of high
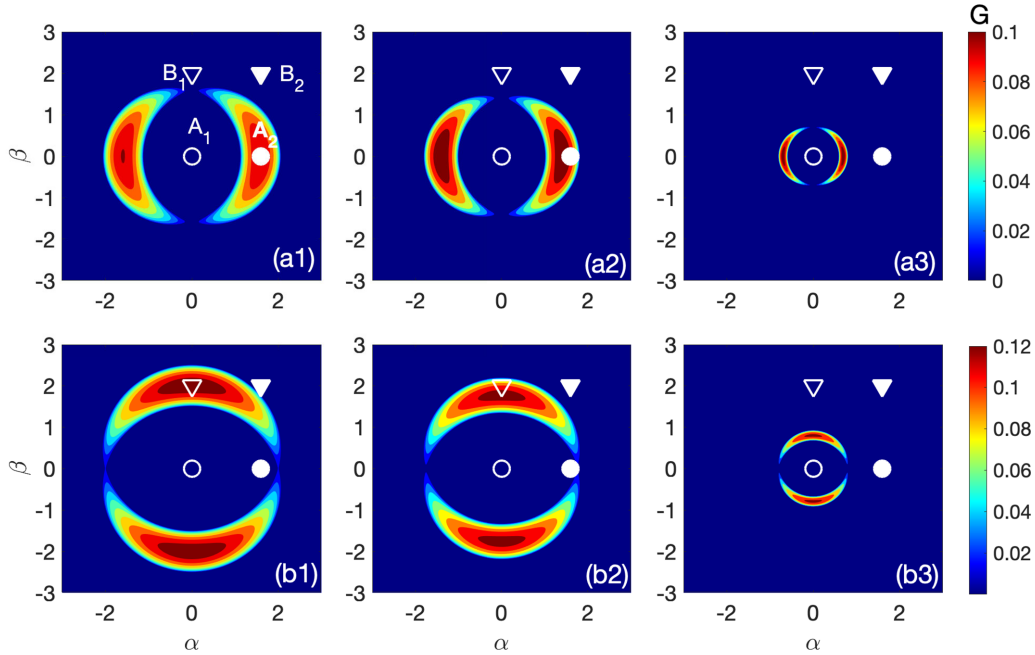
FIG. 2. Contour plot of the MI growth rate distribution in the (α, β) plane, recorded for (a1) $g_0 = 0$, (a2) $g_0 = 0.24$, and (a3) $g_0 = 0.90$, with $g_1 = 4$, $g_2 = 1$, and $g_{12} = 0$ and (b1) $g_0 = 0$, (b2) $g_0 = 0.24$, and (b3) $g_0 = 0.90$, with $g_1 = 4$, $g_2 = 4$, and $g_{12} = 2$; $k = 1$ in all panels. The four modes indicated by A_1, A_2, B_1, and B_2 in (a1) will be of interest in the numerical analysis.

MI gradually diffuse outward from the (α, β) plane when the wave number k increases. The case $g_1 g_2 > g_{12}^2$ presented in Fig. 4 shows similar features, except that for $k = 1$, only two regions of high MI intensity appear. However, in the presence of the residual nonlinearities, with $g_0 = 0.02$, the results are similar to those found in Ref. [68], except that for $k = 3$, the MI distribution of the gain reduces to a ring of instability.

In order to complete this linear stability analysis and reveal the combined effect of the helicoidal SO coupling, the residual nonlinearities, and the perturbation wave number k, the MI gain G is plotted in Fig. 5 in the (k, α) plane for different values of the helicoidal gauge potential β, with $g_1 g_2 < g_{12}^2$ and $g_1 = g_2 > 0$ [see Fig. 5(a)]. Figure 5(b) addresses the same case, but with $g_1 = g_2 < 0$ and $g_{12} < 0$. In the first case, i.e., Fig. 5(a), the immiscibility condition gives rise to regions of instability. For $\beta = 0$, one clearly sees four lobes of instability symmetrical with respect to both the α and k axes. With increasing β, such symmetry in the instability domain is broken in the α direction, with minor lobes appearing for $\alpha < 0$ and lobes of high intensity of the gain getting extended to high values of the gauge amplitude α. Further increasing β, the minor lobes in the area $\alpha < 0$ tend to disappear, letting the MI possibly take place in the upper area $\alpha > 0$ [see Fig. 5(a_3)]. It is clear that in this repulsive case, compared to what was obtained in Ref. [68], the MI growth rate depends on α, particulary in the case $\beta = 0$, where a constant growth rate is obtained. This is confirmed by the spectrum of Fig. 5(b_1), where the central lobes of instability are annihilated by the appearance of high lateral lobes of instability, also distributed to the areas $\alpha < 0$ and $\alpha > 0$. For the rest, when β increases, the MI displays reverse features from the repulsive case. As a whole, the regions of MI in the (k, α) plane are very sensitive to modifications in the gauge potential and the nature of the

interaction, repulsive or attractive, both the traditional and HO interatomic interactions. However, compared to the contributions of Refs. [68,77], combining the helicoidal SO coupling and HO interatomic interactions constitute a promise of richer MI excitation scenarios, in the context where nonlinear and dispersive effects are well balanced.

2. Case of large chemical potential imbalance

In this particular case, most of the calculations are made considering $\kappa \geqslant 1$. In the context where $g_1 = g_2 = 1$ and $g_{12} = 2$, the MI growth rate is represented in Fig. 6(a) in the (k, κ) plane, with the gauge amplitude taking the respective values $\alpha = 0.1$, 0.9, and 2. The instability features show the migration of the maximum growth rate to high values of $|\kappa|$ when α increases. The same behaviors of G are delivered by Fig. 6(b), where $g_1 = g_2 = -1$ and $g_{12} = -2$. In the (k, β) plane, the development of the MI growth rate is displayed in Fig. 7, where Fig. 7(a) shows results for $g_0 = 0.02$, with $g_1 = g_2 = 1$ and $g_{12} = 2$. Here, for the chemical imbalance mismatch if $\kappa = 1$, the instability is supported by four symmetric lobes in both the k and β directions. Recall that, for $\beta < 0$ ($\beta > 0$), the helicoidal SO coupling is right (left) handed. Interestingly, when the mismatch κ gets large, the maximum instability delocalizes to the zone $\beta > 0$, giving favor to the left-handed SO coupling to drive the maximum MI growth rate. The same spectrum of behaviors is shared by Figs. 7(b_1)–7(b_3), where $g_0 = 0.5$, when the right-handed SO coupling is progressively switched off, leaving two major instability bands for $\kappa = 8$ [see Fig. 7(b_3)]. The MI behaviors of Fig. 8 are also of interest, where the MI growth rate exists in the (α, β) plane with the instability bands depending on changes in the interatomic interaction strengths. As a whole,
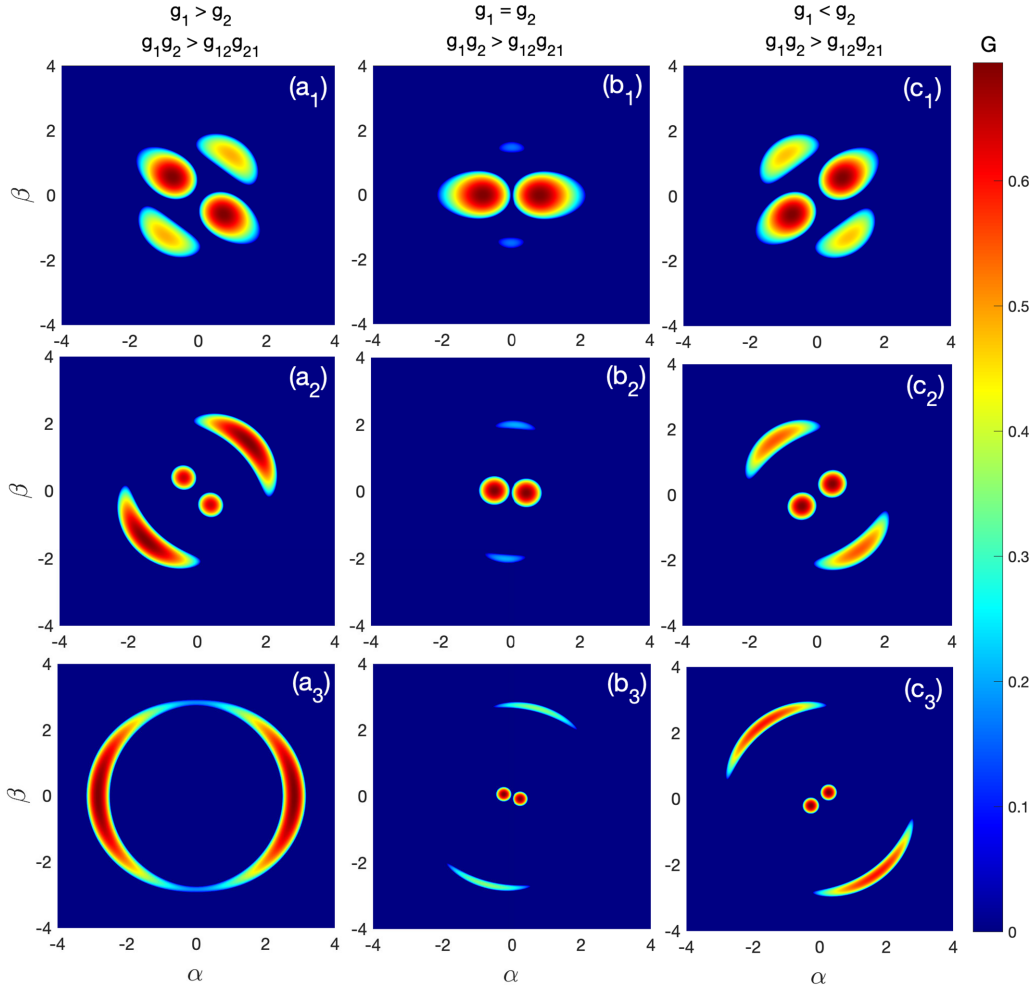
FIG. 3. Contour plot of the MI growth rate distribution in the (α, β) plane for (a) $g_0 = 0.90$, $g_1 = 4$, $g_2 = 1$, and $g_{12} = 0.5$; (b) $g_0 = 0.02$, $g_1 = g_2 = 4$, and $g_{12} = 0.5$; and (c) $g_0 = 0.90$, $g_1 = 1$, $g_2 = 4$, and $g_{12} = 0.5$. From top to bottom, the rows correspond to the perturbation wave numbers $k = 1$, 3, and 5, respectively.

the MI growth rate displays asymmetric instability bands that rotate around the point $(\alpha = 0, \beta = 0)$ for the major lobes to be supported by the β axis. However, for g_0 increasing, the instability areas get smaller, and MI essentially takes place for $\alpha < 0$ and $\beta < 0$ or for $\alpha > 0$ and $\beta > 0$. A similar spectrum of behaviors is delivered by Fig. 9, where the MI growth rate is plotted in the (k, α) plane, with the interatomic interaction strengths varied. Although the instability zone gets expanded for $g_0 = 0.9$, the asymmetric behavior of the MI growth rate is obtained for $g_1 > g_2$ and $g_1 < g_2$, while the maximum growth rate takes place around and at the point $\alpha = 0$.

IV. NUMERICAL EXPERIMENTS

Our analytical predictions obtained in the preceding section are based on linearization and then represent only an approximation of the actual behavior of the system. In order to have a deeper view into the actual dynamics and confirm our predictions on the modulation instability of the system, we perform numerical computations of the governing model in Eqs. (2) and (3). Throughout this section, we take the strength of the Zeeman splitting to be $\Delta = 0.01$ and use $p_{ij} = g_0 g_{ij}$,

where g_0 is positive for all kinds of interactions. This particular choice of the residual nonlinearity strength is expected to preserve the miscibility condition of the system as fixed by the two-body interaction. We use a continuous wave as the initial condition for both components of the condensate and compute the time and space evolution of the wave through the system. For this, we take

$$\psi_1(x, 0) = \psi_2(x, 0) = \sqrt{n_0} + \varepsilon \cos(kx), \qquad (31)$$

where the wave number is $k = 1$. The perturbation amplitude is $\varepsilon = 0.01$, which is small enough compared to the wave amplitude $\sqrt{n_0} = 1.0$ and thus would not cause a qualitative change in the results. The numerically simulated dynamics of the binary BEC is portrayed for selected points in parameters space.

A. Stabilization of miscible mixtures with two-body repulsion

In the case when the strengths of two-body interactions are negative, both stable and unstable dynamics of the system are possible depending on both the miscibility and asymmetry of the two-component system.
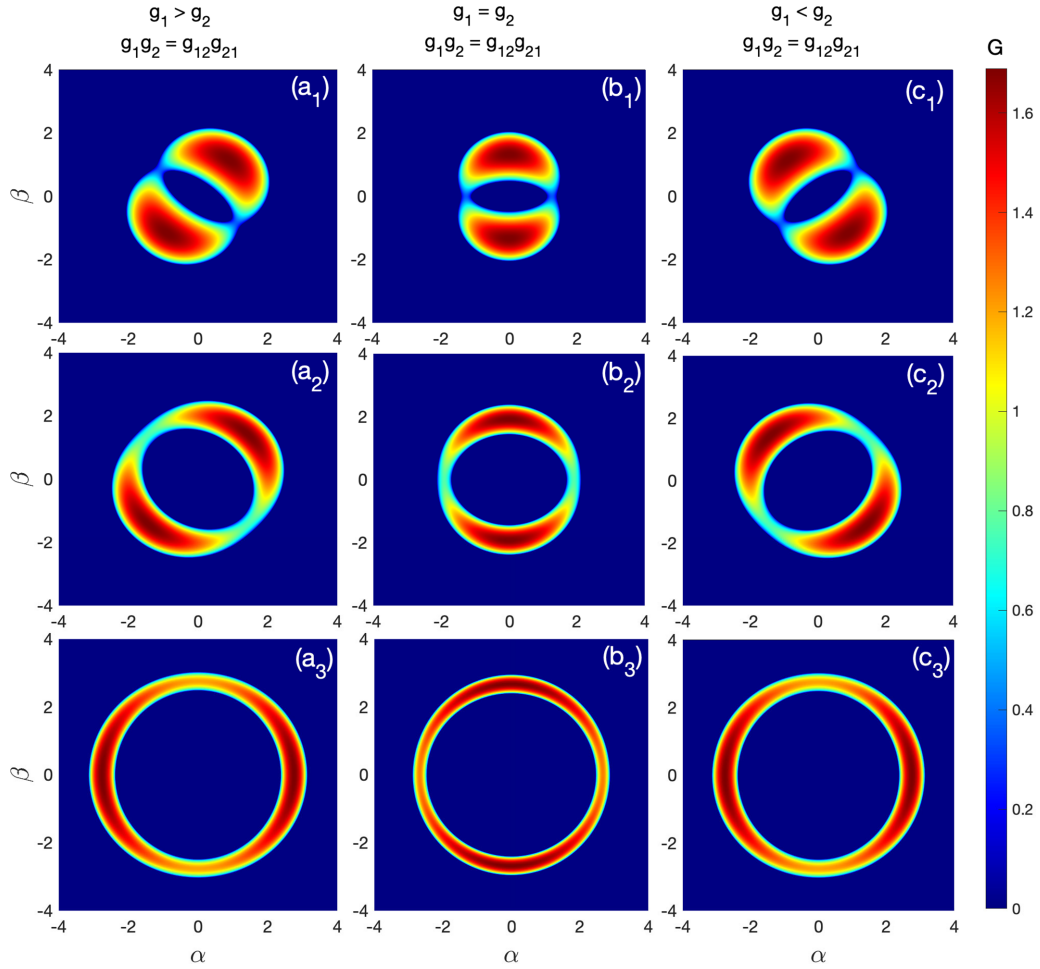
FIG. 4. Contour plot of the MI growth rate distribution in the (α, β) plane for (a) $g_1 = 4$, $g_2 = 1$, $g_{12} = 2$, and $g_0 = 0.90$; (b) $g_1 = g_2 = g_{12} = 2$ and $g_0 = 0.90$; and (c) $g_1 = 1$, $g_2 = 4$, $g_{12} = 2$, and $g_0 = 0.02$. From top to bottom, the rows correspond to the perturbation wave numbers $k = 1$, 3, and 5, respectively.
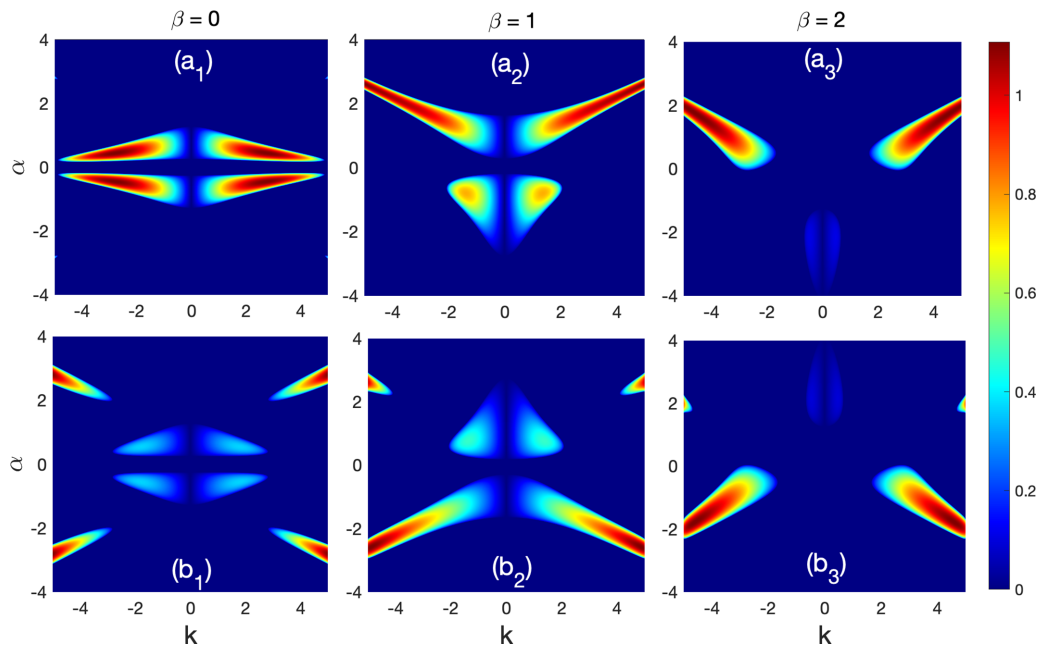

FIG. 5. Distribution of the MI growth rate versus the perturbation wave number k and the gauge amplitude α for (a) $g_0 = 0.90$, $g_1 = g_2 = 1$, and $g_{12} = 2$ and (b) $g_0 = 0.02$, $g_1 = g_2 = -1$, and $g_{12} = -2$. From left to right, the columns correspond to $\beta = 0$, 1, and 2, respectively.
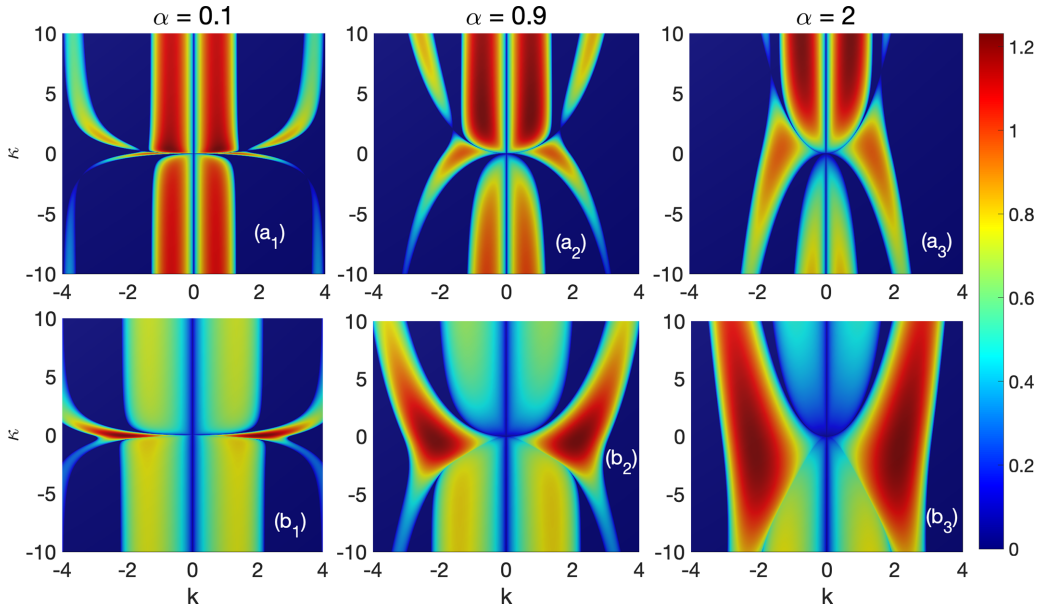
FIG. 6. Distribution of the MI growth rate versus the perturbation wave number k and the frequency mismatch κ for $\beta = 2$, with α taking the respective values of 0.1, 0.9, and 2 for columns from left to right. The helicoidal gauge potential takes the value $\beta = 2$ with (a) $g_0 = 0.90$, $g_1 = g_2 = 1$, and $g_{12} = 2$ and (b) $g_0 = 0.02$, $g_1 = g_2 = -1$, and $g_{12} = -2$.

1. Enhancement of the existing stability

When the strengths of interactions allow the mixture to be miscible, i.e., $g_1 g_1 > g_{12}^2$, one expects the wave propagation in the system to be stable for purely two-body repulsion. Figure 10 shows the dynamics of the wave in the system when only the intraspecies two-body interactions exist. Since the interspecies interaction is absent, the miscibility condition $g_1 g_1 > g_{12}^2$ is always satisfied. As one could expect, the wave propagation in the system is fully stable [see Figs. 10(a1) and 10(a2) for the first and second BEC components,

respectively] when $g_0 = 0$. The maximum amplitude oscillates but remains very close to its initial value. In the presence of residual interaction ($g_0 \neq 0$) as shown in Figs. 10(b1) and 10(b2), the stability of the system is further reinforced as the small modulations which were present in Figs. 10(a1) and 10(a2), though not making the system unstable, have been suppressed in Figs. 10(b1) and 10(b2). The full space-time evolution of the density corresponding to Figs. 10(b1) and 10(b2) is portrayed for the first [Fig. 10(c)] and the second [Figs. 10(d)] species to further appreciate the stability. Similar
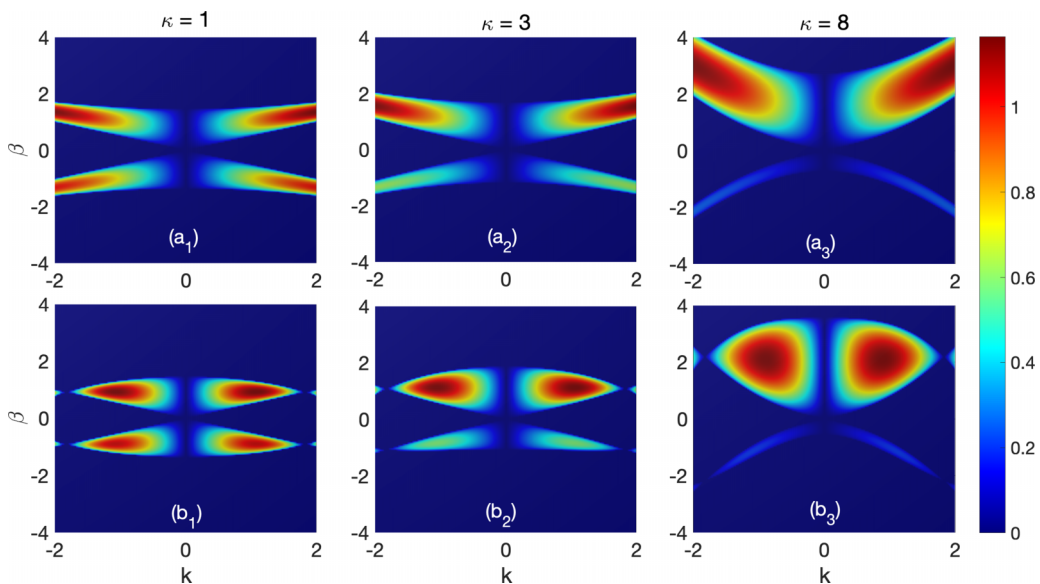

FIG. 7. Distribution of the MI growth rate versus the perturbation wave number k and the helicoidal gauge potential β for $\alpha = 1$, with the frequency mismatch κ taking the respective values 1, 3, and 8 for columns from left to right. The helicoidal gauge potential takes the value $\beta = 2$, with (a) $g_0 = 0.90$, $g_1 = g_2 = 1$, and $g_{12} = 2$ and (b) $g_0 = 0.02$, $g_1 = g_2 = -1$, and $g_{12} = -2$.
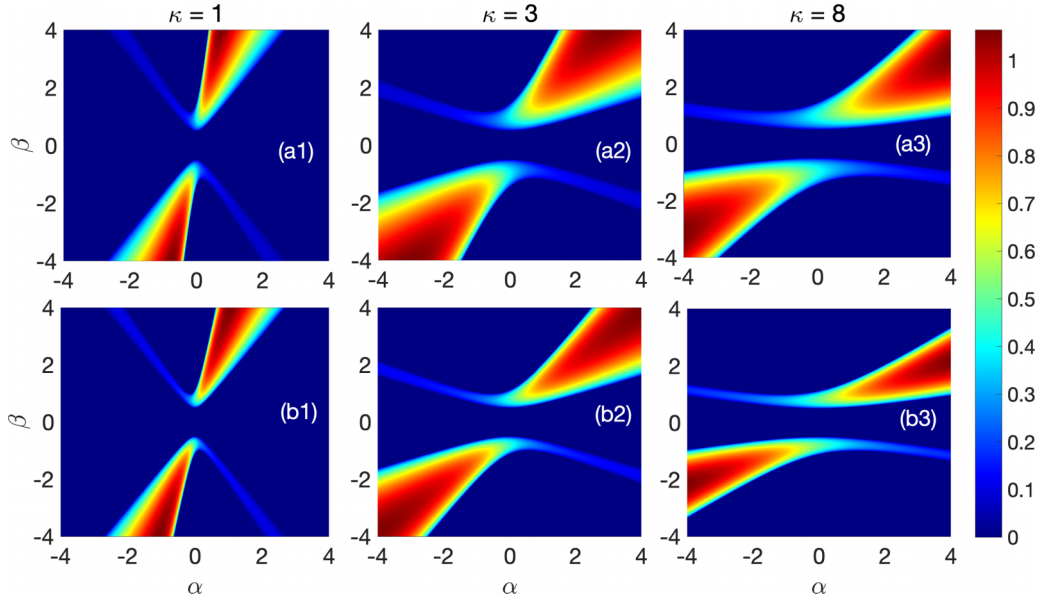
FIG. 8. Distribution of the MI growth rate in the (α, β) plane for a perturbation wave number $k = 1$ and the frequency mismatch κ taking the respective values 1, 3, and 8 for columns from left to right, with (a) $g_0 = 0.02$ and (b) $g_0 = 0.9$. The other parameters are $g_1 = g_2 = 1$, $g_{12} = 2$, and $n_0 = 1$.

behavior can be obtained even when the system has both the intra- and the intercomponent two-body interactions as displayed in Fig. 11 because the miscibility condition is still satisfied. The difference between the interaction strengths g_1 and g_2 seems to play no role in this stability since Figs. 10 and 11, where the system is asymmetric and symmetry, respectively, both display similar dynamics. Hence the residual nonlinearity preserves and reinforces the stability of miscible pairs of condensates with SO coupling. What would happen if the initial state is modulationally unstable is an interesting question.

2. Softening of the existing instability

The evolution of a miscible system with intracomponent two-body interactions and spin-orbit coupling is shown in Fig. 12. The system is modulationally unstable, and asymmetry has been considered as $g_1 \neq g_2$. In the presence of residual nonlinearity, the system is still unstable. This can be seen from the exponential growth in the wave amplitude when g_0 is zero as in Fig. 12(a) and nonzero as in Fig. 12(b). It can equally be seen from the formation of periodic structures in both condensates as shown in Figs. 12(c) and 12(d). However,
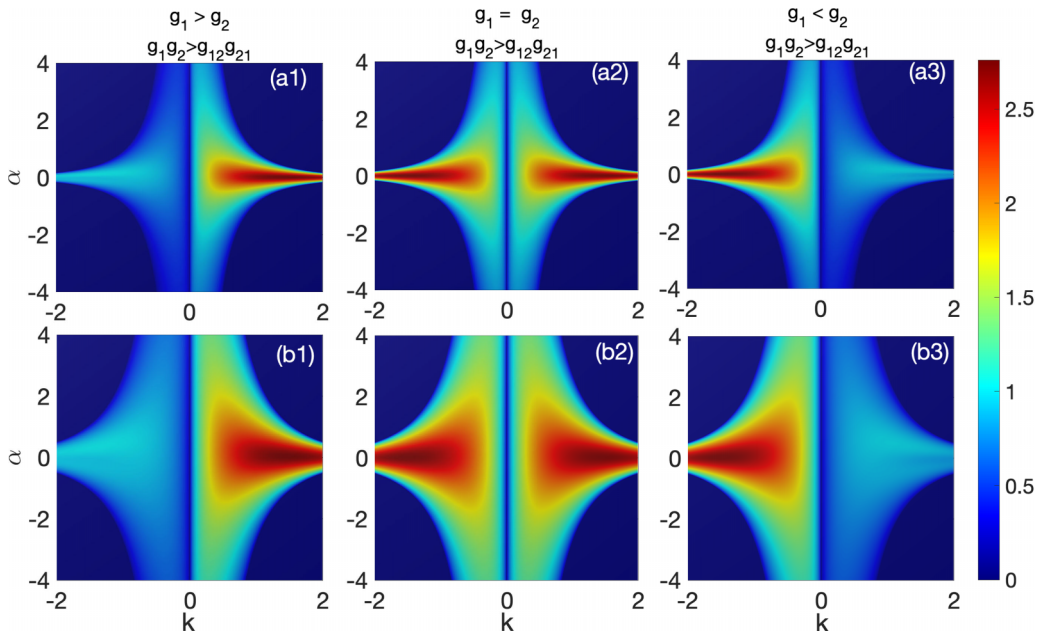

FIG. 9. Distribution of the MI growth rate versus the perturbation wave number k and the gauge amplitude α, with the frequency mismatch $\kappa = 5$ and (a) $g_0 = 0.02$ and (b) $g_0 = 0.9$. From left to right, the columns correspond to $g_1 > g_2$, $g_1 = g_2$, and $g_2 > g_1$, with $g_{12} = 2$.
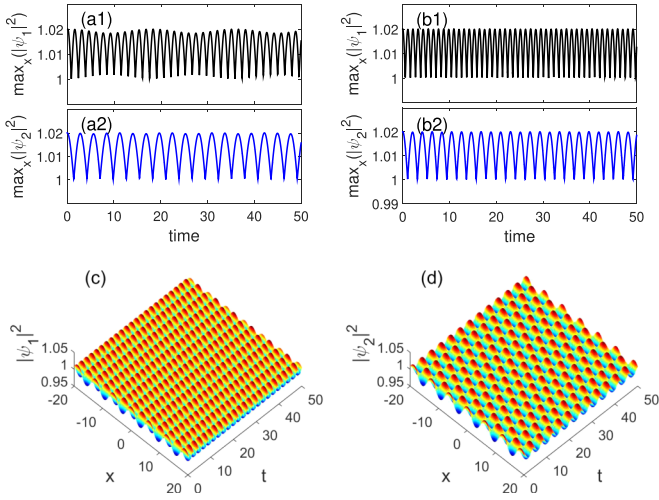
FIG. 10. Numerically computed stable dynamics of the system with only intracomponent two-body interaction. We used $g_0 = 0$, $k = 1$, $g_1 = 4$, $g_2 = 1$, $g_{12} = 0$, $\alpha = \beta = 0$, and (a) $g_0 = 0$ and (b) $g_0 = 1$. Also shown is the space-time evolution of the wave in the (c) first and (d) second species for the same parameters as in (b).

FIG. 12. Numerically computed unstable dynamics of a miscible system with intracomponent two-body interactions and spin-orbit coupling. We used $g_0 = 0$, $k = 1$, $g_1 = 4$, $g_2 = 1$, $g_{12} = 0$, $\alpha = 1.595$, $\beta = 0$, and (a) $g_0 = 0$ and (b) $g_0 = 1$. Also shown is the space-time evolution of the wave in the (c) first and (d) second species for the same parameters as in (b).

the unstable mode exponentially grows only to a smaller maximum amplitude as obtained when comparing Figs. 12(a1) and 12(b1) or Figs. 12(a2) and 12(b2). This corresponds to a reduction of the instability gain and consequently a softening of the MI. Even when the system has both the intra- and the intercomponent two-body interactions and no asymmetry, the same dynamics qualitatively occurs in the system as displayed in Fig. 13, where the system is still miscible. Hence when a miscible binary mixture of condensates with SO coupling is modulationally unstable, the presence of the residual nonlinearity may help soften such an instability.
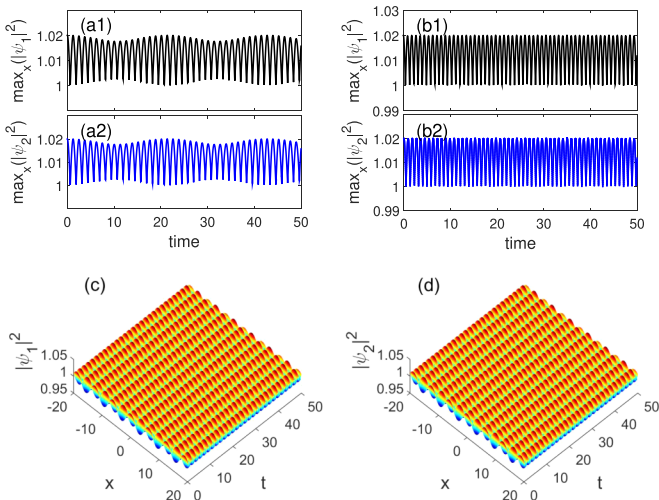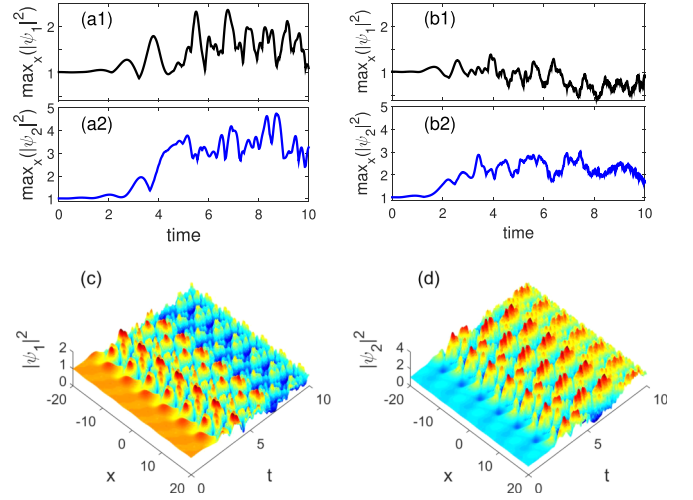
3. Suppression of modulational instability

The softening effect of residual nonlinearity holds the promise of being responsible for the complete stabilization of some unstable modes. That is true, for instance, for a miscible binary condensate system with two-body repulsion. The dynamics of the system is presented in Fig. 14. In the absence of residual nonlinearity, the system is unstable as the amplitude exponentially grows in both condensates [see Figs. 14(a1) and 14(a2)] and periodic structures with high amplitude pulses within both the first [Fig. 14(a3)] and second [Fig. 14(a4)] BEC components. When we consider the residual nonlinearity

FIG. 11. Numerically computed stable dynamics of the system with both intra- and intercomponent two-body interactions. We used $g_0 = 0$, $k = 1$, $g_1 = g_2 = 4$, $g_{12} = 2$, $\alpha = \beta = 0$, and (a) $g_0 = 0$ and (b) $g_0 = 1$. Also shown is the space-time evolution of the wave in the (c) first and (d) second species for the same parameters as in (b).
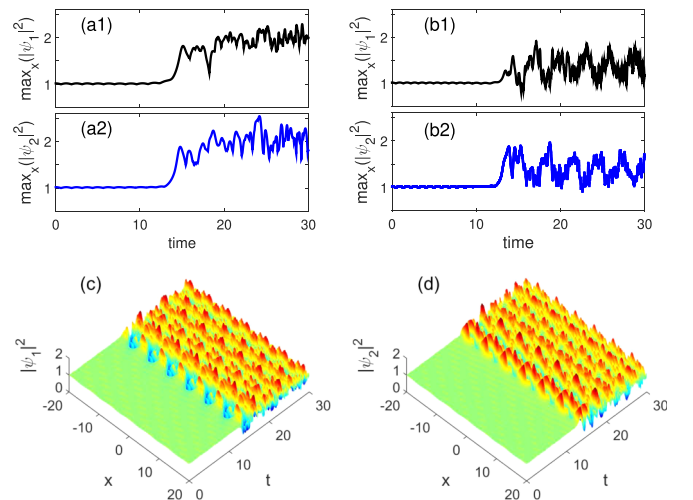

FIG. 13. Numerically computed unstable dynamics of a miscible system with both intra- and intercomponent two-body interactions, residual nonlinearity, and spin-orbit coupling. We used $g_0 = 1$, $k = 1$, $g_1 = g_2 = 4$, $g_{12} = 2$, $\alpha = 1.595$, $\beta = 0$, and (a) $g_0 = 0$ and (b) $g_0 = 1$. Also shown is the space-time evolution of the wave in the (c) first and (d) second species for the same parameters as in (b).
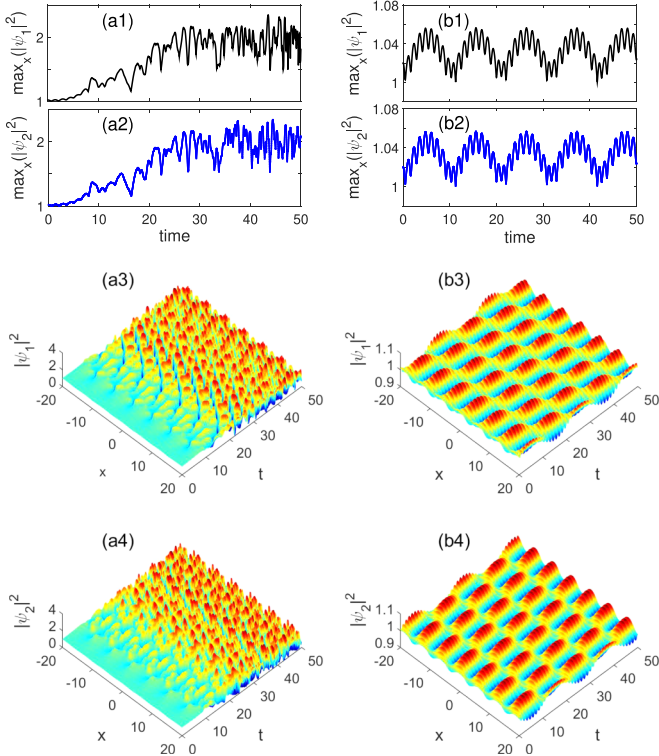
FIG. 14. Numerically computed space-time evolution of the density in both condensate components depicting the suppression of instability in a *miscible* system with two-body repulsion due to the residual nonlinearity. The system is subject to both intra- and intercomponent two-body interactions and the helicoidal gauge potential. We used $k = 1$, $g_1 = g_2 = 4$, $g_{12} = 2$, $\alpha = 0$, $\beta = 1.996$, and (a) $g_0 = 0$ and (b) $g_0 = 1$.

to be nonzero, however, the system becomes modulationally stable as there is no longer exponential growth in the wave amplitude in both condensates [Figs. 14(b1) and 14(b2)]. The perturbed initial plane wave only performs small-amplitude oscillations leading to modulated planelike waves within both the first [Fig. 14(b3)] and second [Fig. 14(b4)] BEC components. The gradual process of stabilization is depicted in Fig. 15. Figure 15(a) shows the density profiles after a runtime $t = 50$, which is long enough to get the onset of MI in the system. As the residual nonlinearity increases, the wave profile evolves and a dramatic change arises around $g_0 = 0.90$ when
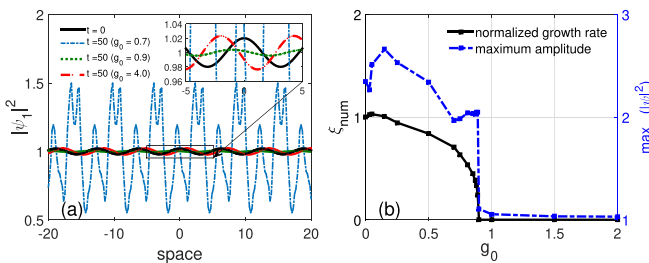

FIG. 15. (a) Density profiles and (b) numerically computed instability growth rate for runs up to $t = 200$ for various values of the residual nonlinearity strengths showing the gradual stabilization of the system. We used $k = 1$, $g_1 = g_2 = 4$, $g_{12} = 2$, $\alpha = 0$, and $\beta = 1.996$.

the profile turns from a train of pulses (blue dash-dotted line) to a regular modulated plane wave (green dotted line). The amplitude of the modulated plane wave is further transformed to make it greater (red dashed line) and then closer to the initial wave (solid black line). From the space-time evolution of the wave, we can extract information about the stable and unstable ranges of residual interaction strengths as well as the information on the instability growth rate. This can be done in several ways, including using the overall maximum amplitude $\max_{x,t}(|\psi|^2)$ or using the time τ_p when the first MI peak occurs. The actual instability growth rate ξ_{num}, displayed in Fig. 15(b) with a black solid line, was calculated as $1/\tau_p$ and normalized to 1 using its value in the limit of zero residual nonlinearity. For $g_0 \geqslant 0.90$, no MI peak was found for runs up $t = 200$ and thus we took $\tau_p = \infty$ for those modes. For increasing g_0, the plot shows a smooth but fast drop in ξ_{num} which makes it comparable to the analytical gain profile. The maximum amplitude is also displayed in Fig. 15(b), depicting a sudden drop from $\max_{x,t}(|\psi|^2) = 2.045$ to 1.108, which is close to the amplitude of the initially perturbed plane wave 1.020. It is obvious that the drop marks the separation between the stable and unstable regions. The maximum amplitude can then allow us to easily distinguish along the g_0 axis a stable range $g_0 \geqslant 0.90$ from an unstable range $g_0 < 0.90$.

Hence, for miscible binary mixtures, the residual nonlinearity can preserve the stability or soften the instability by reducing the growth rate. It can also suppress the instability for safe system parameters, turning unstable modes into completely stable ones.

B. Instability enhancement

1. Case of repulsive interactions

From the above analysis, it is clear that the residual interaction plays an important role in the stabilization of the repulsive two-species BECs even in the presence of spin-orbit couplings and helicoidal gauge potential, provided the miscibility criterion is fulfilled. It is therefore interesting to question whether that stability remains true when the miscibility criterion is no longer satisfied. Figure 16 portrays the dynamics of the first [Fig. 16(a)] and second [Fig. 16(b)] BEC components in the case when $g_1 g_2 < g_{12}^2$, for a symmetrical mixture in the presence of helicoidal gauge potential. The two-body interactions are still repulsive as in the preceding section. In the absence of residual interaction, the dynamics is unstable, as expected for immiscible systems. As done for miscible systems in the preceding section, we consider immiscible systems where the residual interaction is not negligible. Unlike previously, the residual nonlinearity rather destabilizes the system. The onset of the modulational instability in the two-component BEC arises earlier when the strength of residual nonlinearity increases, eventually leading to very high wave amplitudes [see the modes with $g_0 = 0.08$ (green solid line) and 0.09 (magenta dash-dotted line)]. In this case, the formation of periodic structures through the MI process as shown in Fig. 16(c) is accompanied by the gradual separation of the initially mixed species. When pulse trains are formed within the system, the pulses from different species avoid any overlap between them in both the absence [Fig. 16(d1)] and presence [Fig. 16(d2)] of residual nonlinearity.
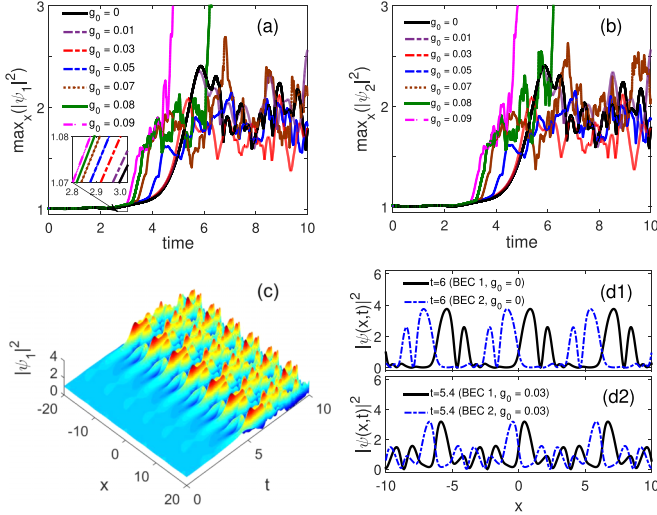
FIG. 16. Numerically computed space-time evolution of the maximum density in the (a) first and (b) second condensate species depicting the destabilizing effect of the residual nonlinearity in an *immiscible* system with two-body repulsion. The system is subject to both intra- and intercomponent two-body interactions and the helicoidal gauge potential. We used $k = 1$, $g_1 = g_2 = 2$, $g_{12} = 4$, $\alpha = 0$, and $\beta = 1.996$. (c) Example of space-time evolution for $g_0 = 0.03$ in the first species and (d) examples of space profiles depicting the immiscibility of generated pulses.
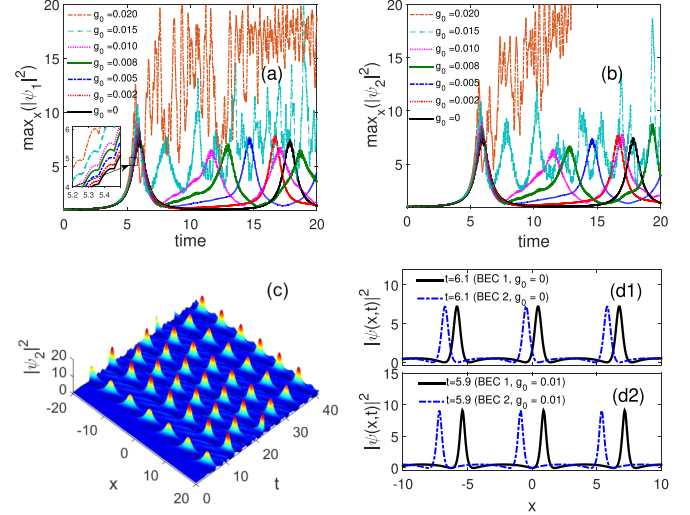

FIG. 17. Numerically computed space-time evolution of the maximum density in both condensate components depicting the destabilizing effect of the residual nonlinearity in a system with two-body attraction. The system is subject to intracomponent two-body interactions and the helicoidal gauge potential. We used $k = 1$, $g_1 = g_2 = -1$, $g_{12} = 0$, $\alpha = 0$, and $\beta = 1.996$. (c) Example of space-time evolution for $g_0 = 0.03$ in the second species and (d) examples of space profiles depicting the Akhmediev-like breathers generated by the MI.

2. Case of attractive interactions

The MI enhancement obtained above for mixtures with two-body repulsion happens to exist also for mixtures with two-body attraction whether they are immiscible or not. To examine that, we consider the interesting situation when the system is miscible and subject to intracomponent two-body interactions and the helicoidal gauge potential. The modulational instability occurs in the two-component BEC even for very weak strengths of residual nonlinearity, as one may see in Fig. 17. When the strength of residual nonlinearity increases, the exponential growth arises earlier and becomes stronger, eventually leading to extremely high wave amplitudes in both BEC components [see the mode with $g_0 = 0.020$ (magenta dash-dotted line) in Figs. 17(a) and 17(b)]. The instability is accompanied by the formation of stable pulse trains as shown in Fig. 17(c). The pulses are regularly spaced by a distance of $2\pi/k$, with $k = 1$ corresponding to the wave number of the injected perturbation. In both the absence [Fig. 17(d1)] and presence [Fig. 17(d2)] of residual nonlinearity, the pulses are Akhmediev-like breathers, as one can readily notice from their shape. Hence the MI-induced formation of stable solitons in mixtures of BECs with two-body attraction may be preserved by the residual nonlinearity even though the latter enhances the instability. We believe that such a result is due to a complex mechanism whose investigation is beyond the scope of this work.

V. CONCLUSION

To summarize, the MI has been addressed in a binary mixture of BECs through a set of coupled GP equations in the presence of HO residual nonlinearities and helicoidal

SO coupling. Through the standard theory of linear stability analysis, we have found the dispersion relation for the perturbation frequency, from which an expression for the MI integrated gain has been proposed. A comprehensive parametric analysis of the instability gain has been carried out, with insistence on the competitive effects between residual nonlinearities, helicoidal SO coupling, and interatomic interactions. Our analysis revealed that the presence of HO interactions supports modulational instability even in miscible two-component condensates, in the context where the gauge potential and the gauge amplitude are suitably chosen. Due to the combination of the residual HO interaction and helicoidal SO effects, it was found that the MI occurrence in immiscible condensates gets importantly modified and responds to gain excitation in both left- and right-handed helicoidal coupling. Such results were found to agree with direct numerical simulations. Due to the residual interaction, the modulational instability is softened and can even be suppressed for miscible binary mixtures with two-body repulsion in the presence of spin-orbit coupling. For immiscible mixtures, however, the modulational instability is enhanced by the residual interatomic interactions.

[1] D. S. Jin, J. R. Ensher, M. R. Matthews, C. E. Wieman, and E. A. Cornell, Phys. Rev. Lett. **77**, 420 (1996).

[2] M.-O. Mewes, M. R. Andrews, N. J. van Druten, D. M. Kurn, D. S. Durfee, C. G. Townsend, and W. Ketterle, Phys. Rev. Lett. **77**, 988 (1996).

[3] D. S. Jin, M. R. Matthews, J. R. Ensher, C. E. Wieman, and E. A. Cornell, Phys. Rev. Lett. **78**, 764 (1997).

[4] S. Stringari, Phys. Rev. Lett. **77**, 2360 (1996).

[5] M. Edwards, P. Ruprecht, K. Burnett, R. Dodd, and C. W. Clark, Phys. Rev. Lett. **77**, 1671 (1996).

[6] D. A. W. Hutchinson, E. Zaremba, and A. Griffin, Phys. Rev. Lett. **78**, 1842 (1997).

[7] M. R. Andrews, D. M. Kurn, H.-J. Miesner, D. S. Durfee, C. G. Townsend, S. Inouye, and W. Ketterle, Phys. Rev. Lett. **79**, 553 (1997).

[8] C. J. Myatt, E. A. Burt, R. W. Ghrist, E. A. Cornell, and C. E. Wieman, Phys. Rev. Lett. **78**, 586 (1997).

[9] M.-O. Mewes, M. R. Andrews, D. M. Kurn, D. S. Durfee, C. G. Townsend, and W. Ketterle, Phys. Rev. Lett. **78**, 582 (1997).

[10] M. C. Cross and P. C. Hohenberg, Rev. Mod. Phys. **65**, 851 (1993).

[11] Y. Li, G. I. Martone, L. P. Pitaevskii, and S. Stringari, Phys. Rev. Lett. **110**, 235302 (2013).

[12] S. Inouye, M. Andrews, J. Stenger, H.-J. Miesner, D. M. Stamper-Kurn, and W. Ketterle, Nature (London) **392**, 151 (1998).

[13] F. K. Fatemi, K. M. Jones, and P. D. Lett, Phys. Rev. Lett. **85**, 4462 (2000).

[14] E. Haller, R. Hart, M. J. Mark, J. G. Danzl, L. Reichsöllner, M. Gustavsson, M. Dalmonte, G. Pupillo, and H. C. Nägerl, Nature (London) **466**, 597 (2010).

[15] L. Deng, E. W. Hagley, J. Wen, M. Trippenbach, Y. Band, P. S. Julienne, J. Simsarian, K. Helmerson, S. Rolston, and W. D. Phillips, Nature (London) **398**, 218 (1999).

[16] M. R. Matthews, B. P. Anderson, P. C. Haljan, D. S. Hall, C. E. Wieman, and E. A. Cornell, Phys. Rev. Lett. **83**, 2498 (1999).

[17] K. W. Madison, F. Chevy, W. Wohlleben, and J. Dalibard, Phys. Rev. Lett. **84**, 806 (2000).

[18] J. R. Abo-Shaeer, C. Raman, J. M. Vogels, and W. Ketterle, Science **292**, 476 (2001).

[19] J. Denschlag, J. E. Simsarian, D. L. Feder, C. W. Clark, L. A. Collins, J. Cubizolles, L. Deng, E. W. Hagley, K. Helmerson, W. P. Reinhardt *et al.*, Science **287**, 97 (2000).

[20] S. Burger, K. Bongs, S. Dettmer, W. Ertmer, K. Sengstock, A. Sanpera, G. V. Shlyapnikov, and M. Lewenstein, Phys. Rev. Lett. **83**, 5198 (1999).

[21] L. Khaykovich, F. Schreck, G. Ferrari, T. Bourdel, J. Cubizolles, L. D. Carr, Y. Castin, and C. Salomon, Science **296**, 1290 (2002).

[22] K. E. Strecker, G. B. Partridge, A. G. Truscott, and R. G. Hulet, Nature (London) **417**, 150 (2002).

[23] F. K. Abdullaev, P. G. Kevrekidis, and M. Salerno, Phys. Rev. Lett. **105**, 113901 (2010).

[24] F. K. Abdullaev, V. V. Konotop, M. Salerno, and A. V. Yulin, Phys. Rev. E **82**, 056606 (2010).

[25] I. Shomroni, E. Lahoud, S. Levy, and J. Steinhauer, Nat. Phys. **5**, 193 (2009).

[26] F. Abdullaev, A. Abdumalikov, and R. Galimzyanov, Phys. Lett. A **367**, 149 (2007).

[27] K. Staliunas, S. Longhi, and G. J. de Valcárcel, Phys. Rev. Lett. **89**, 210406 (2002).

[28] F. K. Abdullaev and M. Salerno, Phys. Rev. A **72**, 033617 (2005).

[29] M. Greiner, O. Mandel, T. W. Hänsch, and I. Bloch, Nature (London) **419**, 51 (2002).

[30] L. Fallani, F. S. Cataliotti, J. Catani, C. Fort, M. Modugno, M. Zawada, and M. Inguscio, Phys. Rev. Lett. **91**, 240405 (2003).

[31] C. Lee, W. Hai, L. Shi, X. Zhu, and K. Gao, Phys. Rev. A **64**, 053604 (2001).

[32] V. M. Eguíluz, E. Hernández-García, O. Piro, and S. Balle, Phys. Rev. E **60**, 6571 (1999).

[33] G. Chong, W. Hai, and Q. Xie, Phys. Rev. E **71**, 016202 (2005).

[34] A. D. Martin, C. S. Adams, and S. A. Gardiner, Phys. Rev. Lett. **98**, 020402 (2007).

[35] G. Chong, W. Hai, and Q. Xie, Phys. Rev. E **70**, 036213 (2004).

[36] H. Saito and M. Ueda, Phys. Rev. Lett. **86**, 1406 (2001).

[37] P. Coullet and N. Vandenberghe, Phys. Rev. E **64**, 025202(R) (2001).

[38] F. T. Arecchi, J. Bragard, and L. M. Castellano, Opt. Commun. **179**, 149 (2000).

[39] V. Zakharov and L. Ostrovsky, Physica D **238**, 540 (2009).

[40] E. V. Goldstein and P. Meystre, Phys. Rev. A **55**, 2935 (1997).

[41] T. S. Raju, P. K. Panigrahi, and K. Porsezian, Phys. Rev. A **71**, 035601 (2005).

[42] N. G. Berloff, Phys. Rev. Lett. **94**, 120401 (2005).

[43] I. Kourakis, P. K. Shukla, M. Marklund, and L. Stenflo, Eur. Phys. J. B **46**, 381 (2005).

[44] M. A. Hoefer, J. J. Chang, C. Hamner, and P. Engels, Phys. Rev. A **84**, 041605(R) (2011).

[45] A. P. Sheppard and Y. S. Kivshar, Phys. Rev. E **55**, 4773 (1997).

[46] C. Hamner, J. J. Chang, P. Engels, and M. A. Hoefer, Phys. Rev. Lett. **106**, 065302 (2011).

[47] J. Stenger, S. Inouye, D. M. Stamper-Kurn, H.-J. Miesner, A. P. Chikkatur, and W. Ketterle, Nature (London) **396**, 345 (1998).

[48] J. Stenger, S. Inouye, A. P. Chikkatur, D. M. Stamper-Kurn, D. E. Pritchard, and W. Ketterle, Phys. Rev. Lett. **82**, 4569 (1999).

[49] T. L. Ho and V. B. Shenoy, Phys. Rev. Lett. **77**, 3276 (1996).

[50] P. Öhberg and S. Stenholm, Phys. Rev. A **57**, 1272 (1998).

[51] E. Timmermans, Phys. Rev. Lett. **81**, 5718 (1998)

[52] H. Pu and N. P. Bigelow, Phys. Rev. Lett. **80**, 1134 (1998).

[53] J. J. García-Ripoll and V. M. Perez-García, Phys. Rev. Lett. **84**, 4264 (2000).

[54] B. D. Esry and C. H. Greene, Phys. Rev. A **59**, 1457 (1999).

[55] M. Eto, K. Kasamatsu, M. Nitta, H. Takeuchi, and M. Tsubota, Phys. Rev. A **83**, 063603 (2011).

[56] M. Kobayashi, Y. Kawaguchi, M. Nitta, and M. Ueda, Phys. Rev. Lett. **103**, 115301 (2009).

[57] T. Kaneda and H. Saito, Phys. Rev. A **90**, 053632 (2014).

[58] K. Sasaki, N. Suzuki, and H. Saito, Phys. Rev. A **83**, 053606 (2011).

[59] T. Kaneda and H. Saito, Phys. Rev. A **93**, 033611 (2016).

[60] K. Kasamatsu, Y. Yasui, and M. Tsubota, Phys. Rev. A **64**, 053605 (2001).

[61] C. K. Law, C. M. Chan, P. T. Leung, and M.-C. Chu, Phys. Rev. A **63**, 063612 (2001).

[62] S. Ishino, M. Tsubota, and H. Takeuchi, Phys. Rev. A **83**, 063602 (2011).

[63] C. Wang, C. Gao, C. M. Jian, and H. Zhai, Phys. Rev. Lett. **105**, 160403 (2010).

[64] Y. Li, L. P. Pitaevskii, and S. Stringari, Phys. Rev. Lett. **108**, 225301 (2012).

[65] X-Q. Xu and J. H. Han, Phys. Rev. Lett. **107**, 200401 (2011).

[66] J. Radić, T. A. Sedrakian, I. B. Spielman, and V. Galitski, Phys. Rev. A **84**, 063604 (2011).

[67] I. A. Bhat, T. Mithun, B. A. Malomed, and K. Porsezian, Phys. Rev. A **92**, 063606 (2015).

[68] X. X. Li, R. J. Cheng, A. X. Zhang, and J. K. Xue, Phys. Rev. E **100**, 032220 (2019).

[69] P. Otlaadisa, C. B. Tabi, and T. C. Kofané, Phys. Rev. E **103**, 052206 (2021).

[70] S. Bhuvaneswari, K. Nithyanandan, P. Muruganandam, and K. Porsezian, J. Phys. B **49**, 245301 (2016).

[71] N. P. Robins, W. P. Zhang, E. A. Ostrovskaya, and Y. S. Kivshar, Phys. Rev. A **64**, 021601(R) (2001).

[72] H. Saito and M. Ueda, Phys. Rev. A **72**, 023610 (2005).

[73] W. Zhang, D. L. Zhou, M.-S. Chang, and M. S. Chapman, Phys. Rev. Lett. **95**, 180403 (2005).

[74] R. S. Tasgal and Y. B. Band, Phys. Rev. A **91**, 013615 (2015).

[75] D. Singh, M. K. Parit, T. S. Raju, and P. K. Panigrahi, J. Phys. B **53**, 245001 (2020).

[76] X.-Y. Qi and J.-K. Xue, Phys. Rev. E **86**, 017601 (2012).

[77] R. Tamilthiruvalluvar, E. Wamba, S. Subramaniyan, and K. Porsezian, Phys. Rev. E **99**, 032202 (2019).

[78] Y. V. Kartashov and V. V. Konotop, Phys. Rev. Lett. **118**, 190401 (2017).

[79] N. T. Zinner and M. Thøgersen, Phys. Rev. A **80**, 023607 (2009).

[80] A. Collin, P. Massignan, and C. J. Pethick, Phys. Rev. A **75**, 013615 (2007).

[81] T. L. Nicholson, S. Blatt, B. J. Bloom, J. R. Williams, J. W. Thomsen, J. Ye, and P. S. Julienne, Phys. Rev. A **92**, 022709 (2015).

[82] T. Franzen, A. Guttridge, K. E. Wilson, J. Segal, M. D. Frye, J. M. Hutson, and S. L. Cornish, Phys. Rev. Res. **4**, 043072 (2022).

[83] S. Tojo, Y. Taguchi, Y. Masuyama, T. Hayashi, H. Saito, and T. Hirano, Phys. Rev. A **82**, 033609 (2010).

[84] E. M. Gutierrez, G. Alves de Oliveira, K. M. Farias, V. S. Bagnato, and P. C. Marques Castilho, Appl. Sci. **11**, 9099 (2021).

[85] H. Xu, W. Cao, J. Zhang, Y. Mo, K. Mi, Z. Yang, Q. Zhang, and P. Lu, Opt. Express **29**, 11342 (2021).

[86] W. Magnus, Comm. Pure Appl. Math. **7**, 649 (1954).

[87] S. Blanes, F. Casas, J. A. Oteo, and J. Ros, Phys. Rep. **470**, 151 (2009).

[88] I. Gilary, N. Moiseyev, S. Rahav, and S. Fishman, J. Phys. A: Math. Gen. **36**, L409 (2003).

[89] K. Jiménez-García, L. J. LeBlanc, R. A. Williams, M. C. Beeler, C. Qu, M. Gong, C. Zhang, and I. B. Spielman, Phys. Rev. Lett. **114**, 125301 (2015).

[90] J. M. Gomez Llorente and J. Plata, Phys. Rev. A **93**, 063633 (2016).

[91] M. Salerno, F. K. Abdullaev, A. Gammal, and L. Tomio, Phys. Rev. A **94**, 043602 (2016).

[92] C. Jiao, J.-C. Liang, Z.-F. Yu, Y. Chen, A.-X. Zhang, and J.-K. Xue, Front. Phys. **17**, 61503 (2022).

[93] L. Fallani, L. De Sarlo, J. E. Lye, M. Modugno, R. Saers, C. Fort, and M. Inguscio, Phys. Rev. Lett. **93**, 140406 (2004).